Journal of Magnetic Resonance 193 (2008) 226–232

Contents lists available at ScienceDirect

Journal of Magnetic Resonance

journal homepage: www.elsevier.com/locate/jmr

Direct ^{13}C-detection for carbonyl relaxation studies of protein dynamics

Gabriela Pasat, John S. Zintsmaster, Jeffrey W. Peng *

Department of Chemistry and Biochemistry, University of Notre Dame, 251 Nieuwland Science Hall, Notre Dame, IN 46556, USA

ARTICLE INFO

Article history:
Received 13 February 2008
Revised 5 May 2008
Available online 9 May 2008

Keywords:
^{13}C-detection
Carbonyl
Protein dynamics
Rotating-frame relaxation
Cross-correlation
Pin1

ABSTRACT

We describe a method that uses direct ^{13}C-detection for measuring rotating-frame carbonyl (^{13}CO) relaxation rates to describe protein functional dynamics. Key advantages of method include the following: (i) unique access to ^{13}CO groups that lack a scalar-coupled ^{15}N–^{1}H group; (ii) insensitivity to ^{15}N/^{1}H exchange-broadening that can derail ^{1}H-detected ^{15}N and HNCO methods; (iii) avoidance of artifacts caused by incomplete water suppression. We demonstrate the approach for both backbone and side-chain ^{13}CO groups. Accuracy of the ^{13}C-detected results is supported by their agreement with those obtained from established HNCO-based approaches. Critically, we show that the ^{13}C-detection approach provides access to the ^{13}CO groups of functionally important residues that are invisible via ^{1}H-detected HNCO methods because of exchange-broadening. Hence, the ^{13}C-based method fills gaps inherent in canonical ^{1}H-detected relaxation experiments, and thus provides a novel complementary tool for NMR studies of biomolecular flexibility.

© 2008 Elsevier Inc. All rights reserved.

1. Introduction

Nuclear magnetic resonance (NMR) spin relaxation experiments now provide unparalleled opportunities for disclosing flexibility–function relationships in isotope-enriched biomolecules. The most common experiments measure relaxation rate constants of ^{15}N [1,2] and carbonyl ^{13}C [3–6] nuclei for the protein backbone, as well as methyl ^{13}C and deuterium (^{2}D) [7–10] nuclei for side-chains. All of these experiments detect the final signal via proton (^{1}H) nuclei. Here, we present an alternative approach, in which the final signal detection takes place on ^{13}C.

Historically, the intrinsically lower sensitivity ^{13}C relative to ^{1}H has discouraged direct ^{13}C-detection for biological macromolecules. However, with the advent of high-field magnets and cryogenically-cooled probes, there is now resurgent interest in direct ^{13}C-detection for biomolecular NMR [11]. Pioneering work in this resurgence includes that of Dötsch and co-workers [11,12], who have developed experiments for protein backbone resonance assignment via detection on ^{13}CO. More recently, Bermel, Luchinat, and Bertini and co-workers have introduced completely proton-less strategies that involve excitation and detection of ^{13}C [13,14]. These previous developments have focused predominantly on resonance assignment and structure determination. By contrast, we explore here the potential for direct ^{13}C-detection to enhance studies of protein functional dynamics. Specifically, we explore ^{13}C-detection pulse schemes that measure spin relaxation rates of ^{13}C carbonyl nuclei (^{13}CO henceforth).

The first protein ^{13}CO relaxation measurements include those of Zuiderweg and co-workers [4,15], Dayie and Wagner [3], Engelke and Rüterjans [16], Allard and Härd [17], and Ernst and co-workers [18]. These studies showed that ^{13}CO relaxation rates are sensitive probes of site-specific backbone dynamics, often displaying more site-to-site variation than complementary ^{15}N measurements. Furthermore, Fischer et al. [15] and Ernst and co-workers [18] showed that joint analyses of ^{13}CO and ^{15}N relaxation measurements could extend the description of backbone dynamics beyond traditional NH order parameters to include locally anisotropic motions [15,18]. More recently, Wang et al. demonstrated ^{13}CO relaxation can expose biomolecular dynamics that are invisible to traditional ^{15}N–^{1}H experiments [19]. Thus, while ^{13}CO relaxation studies are not as widespread as ^{15}N measurements, it is clear their inclusion enables a more comprehensive understanding of protein dynamics.

^{13}C-detection offers a number of advantages for ^{13}CO relaxation measurements. First, it allows access to functionally important ^{13}CO groups that are inaccessible using the standard ^{1}H-detected strategy, the HNCO [20]. Examples of such groups include backbone ^{13}COs of residues preceding Proline (Pro); such residues are of biological interest since Pro-rich sequences often comprise the docking sites mediating protein–protein docking [21]. Further examples are the side-chain ^{13}COs of Aspartate (Asp) and Glutamate (Glu) residues, which participate in electrostatic or hydrogen bond interactions underlying the catalytic mechanisms of therapeutically important enzymes, such as DHFR [22] and HIV–protease [23]. All of these ^{13}COs lack an adjacent scalar-coupled ^{15}N–^{1}H moiety, and are therefore beyond the grasp of HNCO-based approaches. A second advantage of ^{13}C-detection is that the pulse

* Corresponding author. Fax: +1 574 631 6652.
E-mail address: jpeng@nd.edu (J.W. Peng).

1090-7807/$ - see front matter © 2008 Elsevier Inc. All rights reserved.
doi:10.1016/j.jmr.2008.05.003

schemes require fewer extended spin–echo durations, which are typically needed for coherence transfer across small heteronuclear scalar couplings (e.g. $^1J_{NC'} = 15$ Hz). This means less time spent in the transverse plane, and less signal loss for nuclei plagued by short transverse relaxation times. A third advantage is that peptide linkages that are undetectable via ^{15}N–^{1}H HSQC-based relaxation experiments because of severe exchange ^{1}H and ^{15}N broadening may nevertheless be observable via ^{13}CO-detected methods. Finally, ^{13}C-detection obviously avoids artifacts associated with water suppression and radiation damping. The latter can pose practical problems for ^{1}H-detected relaxation pulse schemes that involve significant proton pulsing to average out cross-correlated relaxation effects and *J*-coupling artifacts.

Below, we describe a ^{13}CO-detected pulse experiment for ^{13}CO spin relaxation and apply it to the backbone and side-chain ^{13}CO nuclei in a small protein. We then compare its results to that obtained using more standard HNCO-based methods. Finally, we point to results uniquely provided by the proposed ^{13}CO-detected approach.

2. Methods

Fig. 1 shows our two-dimensional (2-D) pulse scheme for measuring the rotating-frame spin-lattice relaxation rate constant, $R_{1\rho} = 1/T_{1\rho}$ of protein ^{13}CO groups using direct ^{13}CO-detection. We focus on $R_{1\rho}$ because it is sensitive to both the fast ps-ns motions typically associated with order parameters, as well as the slower μs–ms motions typically ascribed to conformational exchange involved in binding and catalysis. The pulse scheme is a simple variation of the ^{13}CO-detected HCACO experiment from Serber et al. [12]. The output is a series of 2-D $^{13}C^{aliph}(\omega_1/t_1) - {}^{13}CO(\omega_2/t_2)$ spectra with the ^{13}CO relaxation rates encoded into the cross-peak intensities.

The magnetization flow begins with polarization transfer from aliphatic protons to their directly-bonded aliphatic carbons, and then coherence transfer to the adjacent ^{13}CO for relaxation and detection. Below, we use C′ and C^{aliph} to denote ^{13}CO and aliphatic ^{13}C spin operators, respectively. The ^{13}C carrier is initially in aliphatic carbon region. The delay Δ refocuses the $^{13}C^{aliph}$ coherences that are antiphase with respect to ^{1}H. For ^{13}COs adjacent to methine groups, such as non-Glycine backbone ^{13}CO nuclei, we set $\Delta = 1/4J_{CH}$. For ^{13}COs adjacent to methylenes, such as the side-chain ^{13}CO of Asp, Glu, Asparagine (Asn), Glutamine (Gln), and backbone Glycine (Gly) ^{13}COs, we set $\Delta = 1/8J_{CH}$. The constant-time period from (**a**) to (**b**) develops antiphase $2C_{xy}^{aliph}C'_z$ coherence, while simultaneously recording the $^{13}C^{aliph}$ chemical shift and refocusing homonuclear $^{13}C^{aliph}$ scalar couplings. By point (**c**), we have two-spin order $2C_z^{aliph}C'_z\cos(\Omega^{aliph}t_1)$ just prior to the relaxation period.

The ^{13}C carrier then jumps to the ^{13}CO region. An adiabatic tan/tanh pulse rotates the ^{13}CO magnetization to a tilt angle Θ relative to the *z*-axis of the rotating-frame [24], where it is then spin-locked via a long continuous-wave pulse of length t_{lock} with rf-field strength $\gamma_C B_1$. In terms of rotating-frame spin operators, the spin-locked spin order is

$$2C_z^{aliph}(C'_x\sin\Theta + C'_z\cos\Theta). \quad (1)$$

The tilt angle Θ is related to the spin-lock field strength, $\gamma_C B_1$, and the detuning $\Delta\Omega$ from the final carrier position of the ^{13}C spin-lock via the familiar relation

$$\tan\Theta = \left|\frac{\gamma_C B_1}{\Delta\Omega}\right|. \quad (2)$$

The spin order shown in Eq. (1) relaxes along its effective rf-field in the rotating-frame for a duration t_{lock} with rate constant $R_{1\rho}^{off}$. $R_{1\rho}^{off}$ can be approximated as the sum [25]

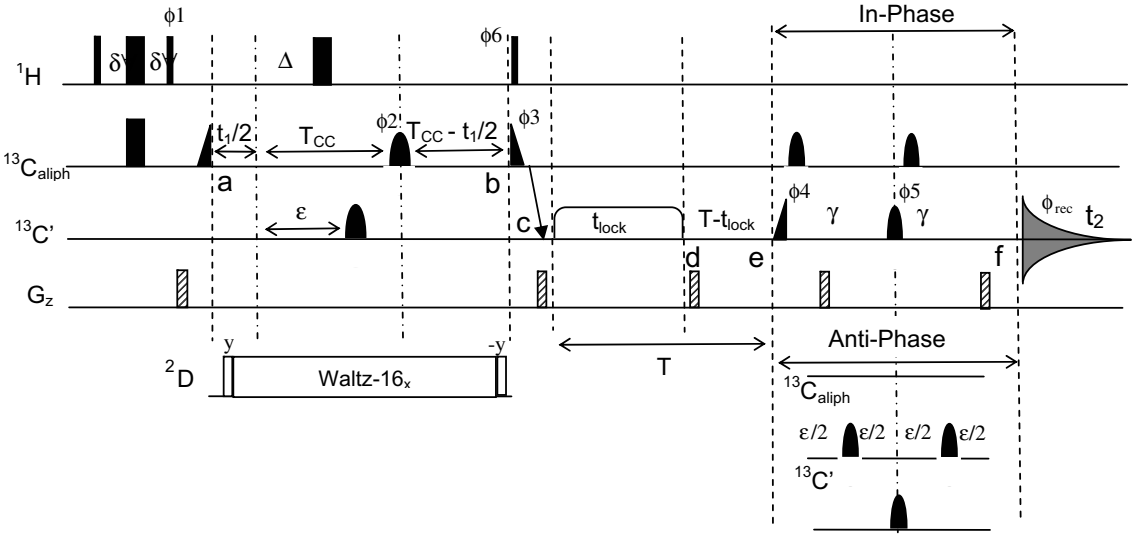

Fig. 1. Pulse scheme for measurement of carbonyl (^{13}CO) rotating-frame relaxation rates using ^{13}C-detection. ^{1}H, $^{13}C_{aliph}$, ^{13}CO, and G_z indicate pulses for proton, aliphatic carbon, carbonyl carbon, and the *z*-gradient. Thin and thick bars indicate rectangular 90- and 180-degree pulses, respectively. Phases are along +*x* unless otherwise noted. Triangular pulses are forward and time-reversed selective Q5 90-degree pulses; half-oval pulses are selective carbon Q3 180-degree pulses [41]. Delays are as follows: $\delta = 1/4J_{CH} = 1.78$ ms, $T_{CC} = 1/2J_{CC} = 13.3$ ms, $\varepsilon = 1/4J_{CaliphC'} = 4.5$ ms, and $\Delta = 1/\{n{*}4J_{CH}\}$. We set $n = 1$ for CH and CHD groups and $n = 2$ for CH_2 groups. Phase increments of ϕ_3 by $\pi/2$ for successive t_1 values provide States-TPPI sign-discrimination in t_1 ($^{13}C^{aliph}$) [42]. Phase cycling is as follows: $\phi_1 = 4(+y), 4(-y)$; $\phi_2 = (x,y,-x,-y)$, $\phi_3 = x$; $\phi_4 = 2(+x), 2(-x)$; $\phi_5 = 4(+x), 4(-x)$; $\phi_6 = y$; $\phi_{rec} = +x, -x, -x, +x, -x, +x, +x, -x$. The IPAP module [26] selects for in-phase (top) or antiphase (bottom) ^{13}CO doublets. The first three gradients were 1ms sine-shaped pulses at 20 g/cm; the last gradient pair were 800 μs sine-shaped pulses at 17 g/cm. The ^{13}C carrier begins on $^{13}C_{aliph}$ (55 ppm for Cα and 35 ppm Cβ), and jumps to the ^{13}CO region at the diagonally downward pointing arrow for spin-locking (176 ppm for backbone and 181 ppm for Glu side-chains). After the longitudinal relaxation delay, $T - t_{lock}$, the carrier jumps to the desired spectral center of the ^{13}CO sweep-width. $R_{1\rho}^{off}$ relaxation occurs during the spin-lock of length t_{lock}, which is bracketed by adiabatic tan/tanh pulses [24]. The delay *T* encompasses the longest spin-lock duration (here, $T = 100$ ms). For partially deuterated proteins, ^{2}D decoupling proceeds during the constant-time period $2T_{CC}$ from (**a**) to (**b**), typically with 1.0 kHz Waltz 16 at 3.5 ppm.

$$R_{1\rho}^{\text{off}} = \sin^2\Theta R_{2z} + \cos^2\Theta R_{zz} + \sin^2\Theta R_{\text{ex}}. \quad (3)$$

In Eq. (3), R_{2z} and R_{zz} are relaxation rate constants describing the decay of $2C_z^{\text{aliph}}C'_{xy}$ and $2C_z^{\text{aliph}}C'_z$, respectively. R_{ex} accounts for additional transverse relaxation (line-broadening) from chemical exchange. After the spin-lock, a time-reversed adiabatic pulse returns the magnetization back to the z-axis (point **d**, Fig. 1) resulting in

$$2C_z^{\text{aliph}}C'_z \cos(\Omega_{\text{aliph}}t_1)\exp\left(-R_{1\rho}^{\text{off}}t_{\text{lock}}\right). \quad (4)$$

Longitudinal relaxation then proceeds for a delay $T - t_{\text{lock}}$, where T is fixed in accordance with the constant relaxation time strategy first introduced by Akke and Palmer [25]. The net relaxation attenuation at point **e** is proportional to

$$\exp\{-R_{zz}(T)\}\exp\left\{-\left(R_{1\rho,\text{eff}}^{\text{off}} - R_{zz}\right)t_{\text{lock}}\right\}. \quad (5)$$

The final ^{13}CO signal is recorded using the in-phase/antiphase (IPAP) strategy of Bax and co-workers [26]. This entails recording complementary pairs of (2-D) in-phase and antiphase spectra for each delay, t_{lock}. Subsequent addition and subtraction yield separate 2-D spectra for the upfield and downfield ^{13}CO doublet components, thus facilitating comparisons of the doublet components' relaxation rates.

For each ^{13}CO doublet, the raw cross-peak intensities for the two components are

$$I^{\pm}(t_{\text{lock}}) = A\exp\left\{-\sin^2\Theta(R_{2z} - R_{zz} + R_{\text{ex}} \pm \eta_{\text{eff}})t_{\text{lock}}\right\}, \quad (6)$$

where "I" is cross-peak intensity, A is an adjustable amplitude factor, and the "+" and "−" denote the upfield and downfield ^{13}CO doublet components, respectively. The term η_{eff} indicates faster relaxation for the upfield versus downfield doublet member due to cross-correlation between the ^{13}CO chemical shift anisotropy (CSA) and ^{13}CO–$^{13}C_{\text{aliph}}$ dipole–dipole (DD) relaxation mechanisms. The pulse scheme of Fig. 1 preserves this doublet relaxation asymmetry since the two $^{13}C^{\text{aliph}}$ 180-degree pulses after the ^{13}CO spin-lock (between **e** and **f**) effectively preserve the doublet component identities. The $\sin^2\Theta$ factor conveniently encapsulates the effects of resonance offset from the spin-lock carrier position, and is one of the *raisons d'être* of the constant relaxation time strategy [25]. Following Eq. (6), extraction of the relaxation rates involves fitting cross-peaks corresponding to each doublet component to a single-exponential decay, and then dividing by $\sin^2\Theta$. This produces for each ^{13}CO doublet two resonance-offset corrected relaxation rates: R_{eff}^{+} for the upfield component, and R_{eff}^{-} for the downfield component.

For each ^{13}CO doublet, we take the difference and sum of R_{eff}^{+} and R_{eff}^{-}. From the difference, we get

$$\eta_{\text{eff}} = \frac{1}{2}\left(R_{\text{eff}}^{+} - R_{\text{eff}}^{-}\right). \quad (7)$$

The η_{eff} term is an effective estimate of the CSA–DD cross-correlation that is actually the difference between CSA–DD terms for the transverse plane and the z-axis, $\eta_{xy} - \eta_z$. The value obtained must be interpreted with caution since Eq. (7) implicitly assumes that cross-relaxation between the two ^{13}CO doublet components is negligible.

From the sum of R_{eff}^{+} and R_{eff}^{-}, we get

$$R_{2,\text{eff}} = \frac{1}{2}\left(R_{\text{eff}}^{-} + R_{\text{eff}}^{+}\right) = (R_{2z} - R_{zz}) + R_{\text{ex}} = (R_2 - R_1) + R_{\text{ex}}, \quad (8)$$

which is an effective transverse relaxation rate constant. The interference term η_{eff} drops out in Eq. (8), and so $R_{2,\text{eff}}$ is free from CSA–DD cross-correlation effects. Note also that Eq. (8) makes the approximation $R_{2z} - R_{zz} = R_2 - R_1$. This is reasonable since, to a good approximation, $R_{2z} \approx R_2 + \rho_{\text{Ca}}$ and $R_{zz} \approx R_1 + \rho_{\text{Ca}}$ [27]. The ρ_{Ca} term is longitudinal $^{13}C^{\text{aliph}}$ relaxation that stems from the dependence of the antiphase two-spin order (cf. Eq. (1)) on the $^{13}C_{\text{aliph}}$ spin state. Since ρ_{Ca} contributes identically to both R_{2z} and R_{zz}, it dies in the difference afforded by constant relaxation time approach.

An alternative pulse scheme could first refocus to in-phase carbonyl magnetization prior to the spin-lock period at point **c**. However, this would mean introducing another spin–echo period of length 2ε (as used for the IPAP module). By approximating $R_{2z} - R_{zz} = R_2 - R_1$, we can use a shorter experiment, which could be beneficial for ^{13}CO nuclei with shorter transverse relaxation times.

3. Results

We acquired the majority of our spectra at 278 K on a 16.4 T (700 MHz ^{1}H Larmor frequency) Bruker Avance system, equipped with a cryogenically cooled inverse-detection triple-resonance TCI probe, in which the ^{1}H coil is closest to the sample, and both the ^{1}H and ^{13}C pre-amplifiers are cold. The protein sample consisted of uniformly ^{13}C and ^{15}N labeled (U–^{13}C/^{15}N) WW domain of human Pin1 (39 residues) dissolved to 0.6 mM in aqueous buffer (90% H_2O, 10% D_2O, 20 mM P_i, 30 mM NaCl, 0.05% NaN_3, pH 7.0). Our previous backbone ^{15}N R_1 and R_2 measurements at 278 K gave an overall rotational correlation time of $\tau_c = 4.43 \pm 0.02$ ns/rad [28]. We also acquired relaxation spectra for full-length, 50% perdeuterated, U–^{13}C/^{15}N human Pin1 (163 residues, 18.5 kDa) at 295 K on an 18.8 T (800 MHz ^{1}H Larmor frequency) Bruker Avance system, also equipped with a cryogenically cooled TCI probe. The full-length Pin1 sample was at 0.7 mM in aqueous buffer (90% H_2O, 10% D_2O, 30 mM imidazole–D_4, 30 mM NaCl, 5 mM DTT-D_{10}, 0.05% NaN_3, pH 6.6). Our previous ^{15}N R_1 and R_2 measurements at 295 K gave rotational correlation times of $\tau_c = 10.7 \pm 0.1$ ns/rad and 15.4 ± 0.2 ns/rad for two flexibly linked WW and isomerase domains of Pin1 [29].

Fig. 2 shows a representative 2-D spectrum of U–^{13}C/^{15}N labeled WW domain from human Pin1 (Pin1–WW hereafter) using the pulse scheme of Fig. 1. It was recorded with $\Delta = 1/4J_{\text{CH}}$ to select for backbone ^{13}CO groups adjacent to methines (CHs); this includes the backbone ^{13}COs of all residues except Gly. The spectrum is the result of adding the in-phase and antiphase spectra for $t_{\text{lock}} = 28$ ms. We assigned the cross-peaks using ^{1}H–^{1}H NOESY spectra along with ^{13}C-detected CBCACO, H(CA)CO spectra. For backbone Gly and side-chain Glu ^{13}CO nuclei, we recorded analogous relaxation measurements with $\Delta = 1/8J_{\text{CH}}$.

The relaxation series included 9 pairs of in-phase and antiphase 2-D spectra, with spin-lock durations $t_{\text{lock}} = 8$ (2×), 16, 28, 38, 48, 68, 78, and 88 ms, resulting in 2.75 days of instrument time on a 700 MHz spectrometer. The spin-locks and their bracketing adiabatic tan/tanh pulses [24] were written as single pulses using in-house software, and then transferred to the spectrometer. The adiabatic sweeps began 26,000 Hz downfield of the final spin-lock position and terminated at the downfield boundary of the ^{13}CO spectral width. The spin-lock amplitude was $\gamma_C B_1/2\pi = 2$ kHz, which calibrated by measuring the resonance offset dependence of the residual $^1J_{\text{HC}}$ splitting of a well-resolved proton signal during continuous-wave ^{13}C decoupling [30]. To ensure constant rf-heating across the relaxation series, we applied preamble spin-locks at the beginning of the sequence (not shown in Fig. 1) [31]. The ^{13}CO sweep-width was 30 ppm (5297 Hz) sampled with 512 points, while the indirect $^{13}C_{\text{aliph}}$ sweep-width covered 28.4 ppm (5000 Hz) sampled by 64 complex points. The in-phase and antiphase datasets were Fourier-transformed separately, and then added and subtracted to yield the up-field and down-field resonances. Cross-peaks were then integrated and fit to single-exponential decays using the Levenburg–Marquardt algorithm and in-house software [32].

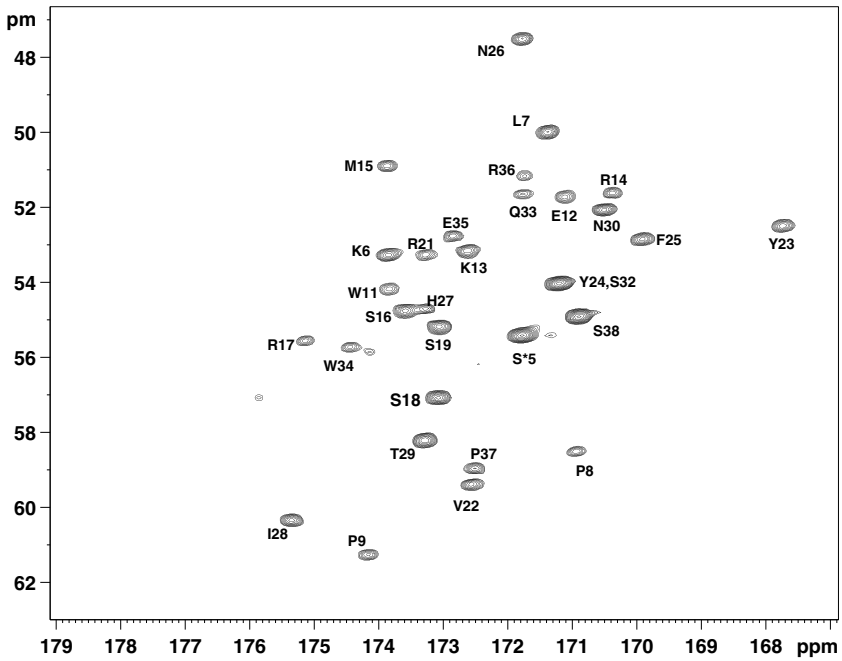

Fig. 2. Example of a 2-D $^{13}C\alpha(\omega_1/t_1) - {}^{13}CO(\omega_2/t_2)$ spectrum for the Pin1–WW domain dissolved to 0.6 mM in 90% H_2O buffer, 278 K, 16.4 T using the ^{13}CO-detection relaxation pulse scheme of Fig. 1. $\Delta = 1/4J_{CH}$ for backbone ^{13}CO groups (excluding those of Gly) and the spin-lock duration is 28 ms with an rf-field strength of $\gamma_C B_1/2\pi = 2$ kHz. Small unlabeled peaks come from a small amount of degraded protein, and the S*5 cross-peak is a Serine from the N-terminal thrombin cut-site that is not part of the Pin1–WW sequence.

The top two panels of Fig. 3 show exemplary decay curves for the backbone ^{13}COs of Glu12 and Ser19. We point out that the backbone NH of Ser19 is absent in standard 2-D ^{15}N–^{1}H relaxation spectra (e.g. ^{15}N R_2 and R_1) because of severe exchange-broadening [28]. Yet, its $^{13}C^{aliph} - {}^{13}C'$ cross-peak is clearly evident in Fig. 2; this reveals ^{13}CO observation as a viable alternative to standard $^{15}N/^{1}H$ methods for gaining access to peptide planes plagued by excessive $^{15}N/^{1}H$ exchange-broadening.

We note in passing that the curve fit quality is limited by the signal-to-noise; thus, it can be improved by increasing the number of scans, or adding the in-phase and antiphase peak intensities (*vide infra*). We remind the reader, however, that a chief purpose of this direct ^{13}C-detected method is to provide signal for reso-

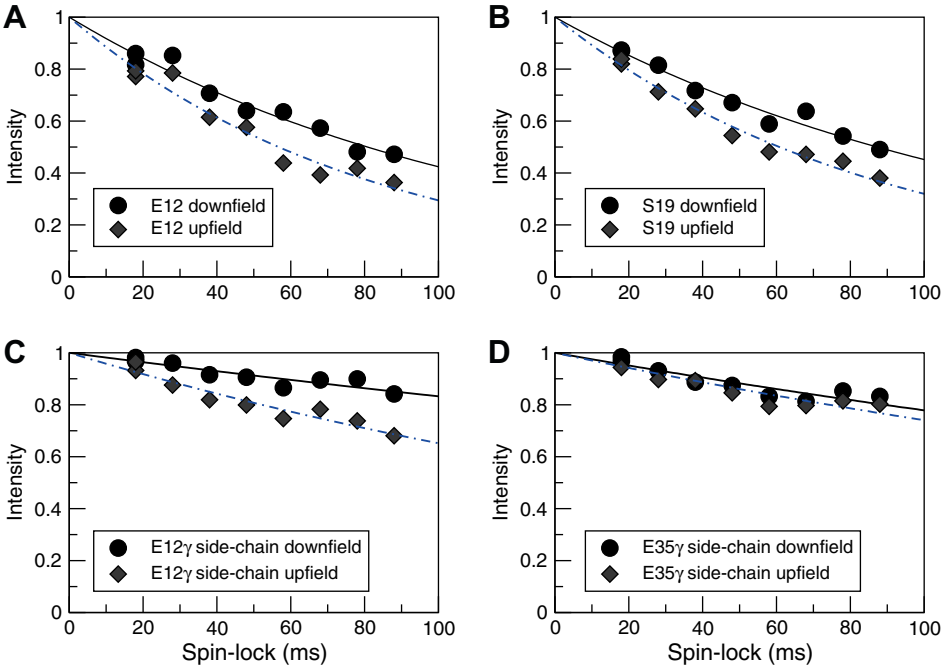

Fig. 3. Exemplary relaxation curves for backbone ^{13}CO of Glu12 (A) Ser19 (B) and the side-chain ^{13}CO groups of Glu12 (C) and Glu35 (D). Circles and diamonds track the decay of the downfield and upfield ^{13}CO doublet components, respectively.

nances (such as Ser19) that would be otherwise invisible using ^{1}H-detected approaches.

The bottom two panels of Fig. 3 show exemplary decay curves for side-chain Glu ^{13}COs using the same spin-lock durations as used for the backbone. These side-chain ^{13}CO nuclei show much less decay, and longer spin-lock durations would be required for more accurate extraction of relaxation rates. Nevertheless, the slower decay shows that these ^{13}C-detected experiments are sensitive to the greater flexibility of the side-chain ^{13}CO moieties relative to those of the backbone. Also, these experiments provide unique access to side-chain ^{13}COs lacking adjacent ^{15}N–^{1}H moieties—a feature that places them beyond the grasp of standard ^{1}H-detected HNCO-based methods [33].

Using Eqs. (2) and (6), we corrected the raw relaxation rate constants for resonance offset effects. We then obtained η_{eff} and $R_{2,\text{eff}}$ using Eqs. (7) and (8). Fig. 4A shows the results for backbone ^{13}CO versus sequence. The solid bars are $R_{2,\text{eff}}$, while the hatched bars are η_{eff}. The trimmed mean of $R_{2,\text{eff}}$ (the mean after removing values outside of one standard deviation from the raw mean) and its standard deviation is $11.3\ \text{s}^{-1} \pm 1.1\ \text{s}^{-1}$. The trimmed mean and standard deviation for η_{eff} is $1.8\ \text{s}^{-1} \pm 0.4\ \text{s}^{-1}$. Thus, while η_{eff} is significant, it is clearly smaller than $R_{2,\text{eff}}$. Results for Lys13 and Ala31, as well as Tyr24 and Ser32 were not possible due to resonance overlap.

To check the accuracy of our ^{13}CO-detected $R_{2,\text{eff}}$ results, we compared them with those obtained using the canonical $^{1}H^{N}$-detected HNCO approach [3,33,34]. Fig. 4B shows a residue-by-residue comparison for the backbone ^{13}CO of Pin1–WW. The darker and lighter bars are $R_{2,\text{eff}}$ values we obtained using the ^{13}CO-detected pulse scheme, and a recent HNCO-based method [34], respectively. Critically, we used identical adiabatic spin-locking pulses, spin-lock durations, ^{13}CO carrier positions, and resonance offset correction formulae (cf. Eqs. (2) and (6)). Hence, as far as ^{13}CO relaxation period is concerned, the only differences between the ^{13}CO-detected and HNCO-based methods are (i) the HNCO-based approach spin-locks in-phase $^{13}C'$ magnetization; (ii) the HNCO-based approach takes no explicit measures to eliminate the cross-correlated relaxation interference term, η_{eff}. Fig. 4B shows that for the vast majority of ^{13}CO resonances, the two approaches give the same results, within the estimated statistical errors (~5%). In fact, the trimmed mean and standard deviation for the HNCO-based $R_{2,\text{eff}}$ is $11.4 \pm 0.6\ \text{s}^{-1}$; this agrees very well with the ^{13}CO-detected results of $11.3 \pm 1.1\ \text{s}^{-1}$ (*vide supra*). Missing slots in the HNCO-based approach are either due to resonance overlap, or severe ^{15}N exchange-broadening that obliterates the resonance in HNCO spectra (e.g. the Ser18 CO is missing because of severe exchange-broadening of Ser19 NH). The largest $R_{2,\text{eff}}$ differences that are beyond the estimated errors occur for Gly ^{13}COs; the HNCO values are about 15% smaller than ^{13}CO-detected values. The origins of these differences are presently unclear, and are the subject of current investigation.

It is instructive that the ^{13}CO-detected $R_{2,\text{eff}}$ values agree well with those from the HNCO-based approach, despite the fact that ^{13}CO-detected approach corrects for CSA–DD cross-correlation effects, while the HNCO-based approach does not. In fact, since the HNCO does not resolve the ^{13}CO doublet members, simply integrating the entire in-phase doublets of the in-phase ^{13}CO-detected spectra should give $R_{2,\text{eff}}$ values in close agreement with those from the HNCO. This is, in fact, the case (data not shown). The agreement is because of the small magnitudes of η_{eff} relative to $R_{2,\text{ eff}}$ (cf. Fig. 4A). While the relaxation of the entire doublet (as detected in the HNCO-based approach) is in principle tainted by bi-exponential decay due to differential relaxation rates of the ^{13}CO doublet components, the difference, η_{eff}, is small compared to $R_{2,\text{eff}}$. As a result, one recovers apparent rate constants that are nearly identical to the "clean" $R_{2,\text{eff}}$ values. Note that integrating the entire in-phase doublet is equivalent to summing the peak integrals of upfield and downfield doublet components for each ^{13}CO. This summation procedure, first demonstrated in ^{13}C-detected HCACO experiments [35], retains resolution and increases the signal-to-noise by approximately $\sqrt{2}$. The resulting gain in signal-to-noise

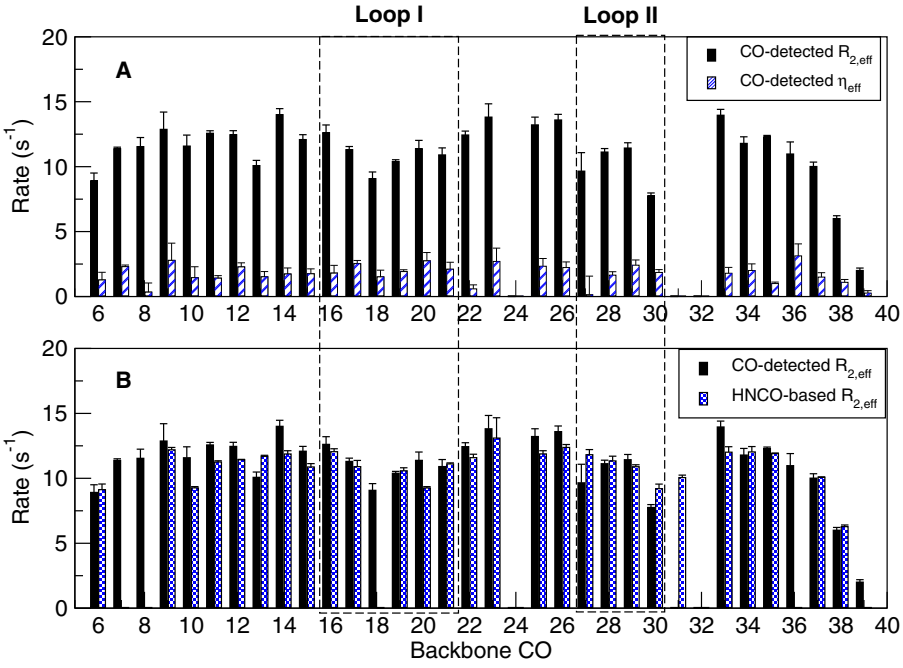

Fig. 4. ^{13}CO relaxation rates versus backbone sequence for the Pin1–WW domain, 0.6 mM, 16.4 T, 278 K. Top (A) juxtaposes $R_{2,\text{eff}}$ and cross-correlation interference term, η_{eff} versus sequence. The η value is typically about 20% that of $R_{2,\text{eff}}$. Bottom (B) juxtaposes $R_{2,\text{eff}}$ (cf. Eq. (8), main text) from the ^{13}CO-detected method of Fig. 1 in darker bars, and the standard HNCO-based method in lighter bars. The average estimated uncertainty is ~5%.

should enhance the quality of curve fits (cf. Fig. 3) and resulting relaxation rates.

4. Discussion

Having addressed the accuracy of the relaxation rates from our ^{13}C-detection method, we can now discuss the information disclosed by such measurements. In doing so, we point out the information uniquely available from the ^{13}C-detection approach.

In Figs. 4A and B, two locales of lower ^{13}CO $R_{2,\mathrm{eff}}$ deserve attention. The first locale includes Ser18 and Ser19 within binding loop I (residues 16–21), whose amino acid sequence determines the binding preferences of WW domains [21]. The lower ^{13}CO $R_{2,\mathrm{eff}}$ values suggest enhanced local mobility, and this is consistent with our previous ^{15}N measurements that showed intrinsic loop I flexibility [28]. The second region of lower ^{13}CO $R_{2,\mathrm{eff}}$ His27 and Asn30. These residues form the boundaries of loop II. Here, the ^{13}CO data suggests enhanced mobility not evident from the previous ^{15}N analyses.

A compelling advantage of ^{13}C-detected ^{13}CO relaxation is that it can provide access to peptide linkages suffering severe ^{15}N–^{1}H exchange-broadening, and thus, are unobservable via ^{1}H-detected 2-D^{15}N or HNCO-based methods. The contiguous stretch Ser16, Arg17, Ser18, and Ser19 in the Pin1–WW domain illustrates this vividly. These are critical residues within the flexible specificity loop I that mediate binding. The intrinsic flexibility causes strong exchange-broadening for the NH resonances of Arg17, Ser18, and Ser19, resulting in little or no signal in pulse schemes having long periods of transverse ^{15}N magnetization. Even at 278 K (which salvages most loop I resonances), Ser18 and Ser19 show no signal in HNCO-based ^{13}CO relaxation pulse schemes. And in standard 2-D ^{5}N R_2 and R_1 spectra, Ser18 is quite faint and Ser19 is completely missing. In contrast, in the ^{13}CO-detected experiment of Fig. 1, all ^{13}CO resonances of binding loop I are clearly present (cf. Fig. 2). This makes sense when we recall that a given exchange process can cause different extents of exchange-broadening for ^{15}N–^{1}H nuclei versus their adjacent ^{13}CO nuclei, because of differences in the ranges and determinants of their chemical shifts. Exchange processes that obliterate ^{15}N–^{1}H resonances may still leave the resonances of adjacent ^{13}CO nuclei intact. Hence, the ^{13}C-detected methods provide unique access to docking loop residues that would be otherwise inaccessible using HN detection approaches. Moreover, since protein–protein interactions are often mediated by flexible or unstructured loops prone to exchange-broadening [36,37], the situation here is likely present in many other docking proteins. This further underscores the complementary benefits of the ^{13}CO-detected relaxation methods.

The ^{13}C-detection approach also provides unique access to the side-chain ^{13}COs of Asp and Glu, which often serve mechanistic roles in enzyme active sites. In contrast to Asn and Gln, these side-chain ^{13}COs do not have adjacent scalar-coupled ^{15}N–^{1}H moieties, and so HNCO approaches are not viable. To detect these side-chain ^{13}COs, we set $\Delta = 1/8J_{\mathrm{CH}}$ (cf. Fig. 1) select for the ^{13}COs adjacent to methylene (CH_2) groups. The constant-time period of $1/J_{\mathrm{CC}}$ lends a $\cos^n(\pi)$ dependence to the cross-peak intensity, where 'n' is the number of carbons bonded to the aliphatic carbon adjacent to the ^{13}CO. Hence, backbone Gly resonances are easily distinguished from those of side-chain Asp, Glu, Asn, and Gln ^{13}COs by their opposite signs. Fig. 3 shows examples of rate constants for Glu12 and Glu35. Their relaxation rates are considerably smaller than those of the backbone, most likely reflecting their enhanced local mobility.

The ^{13}C-detection method of Fig. 1 should also be applicable for dynamics studies of side-chain Asp, Glu, Asn, and Gln, as well as backbone Gly ^{13}CO groups in medium-sized proteins 50% deuterium (^{2}D) and U–^{13}C labeling. To investigate this possibility, we have begun measurements of side-chain ^{13}CO relaxation in full-length 50% ^{2}D, U–^{13}C/^{15}N human Pin1 (163 amino acids, 18.5 kDa). We set $\Delta = 1/4J_{\mathrm{CH}}$ to select for ^{13}COs next to ^{13}CHD methylene isotopomers, and used ^{2}D decoupling during the constant-time period. Fig. 5 shows our initial results for a 0.7 mM human Pin1 sample at 295 K, 18.8 T. The figure zooms in a region containing cross-peaks of Glu side-chain ^{13}Cγ-^{13}CO for Glu. ^{13}CO $R_{2,\mathrm{eff}}$ values, estimated from

$$R_{2,\mathrm{eff}} = \frac{-1}{(\sin^2\Theta)\Delta t_{\mathrm{lock}}} \ln\left\{\frac{I(t_{\mathrm{lock}} = 88\ \mathrm{ms})}{I(t_{\mathrm{lock}} = 18\ \mathrm{ms})}\right\} \tag{9}$$

are indicated next to the boxed cross-peaks. I(88 ms) and I(18 ms) are the cross-peak intensities for $t_{\mathrm{lock}} = 18$ and 88 ms, and $\Delta t_{\mathrm{lock}} = 70$ ms. While the sequence-specific assignments for the

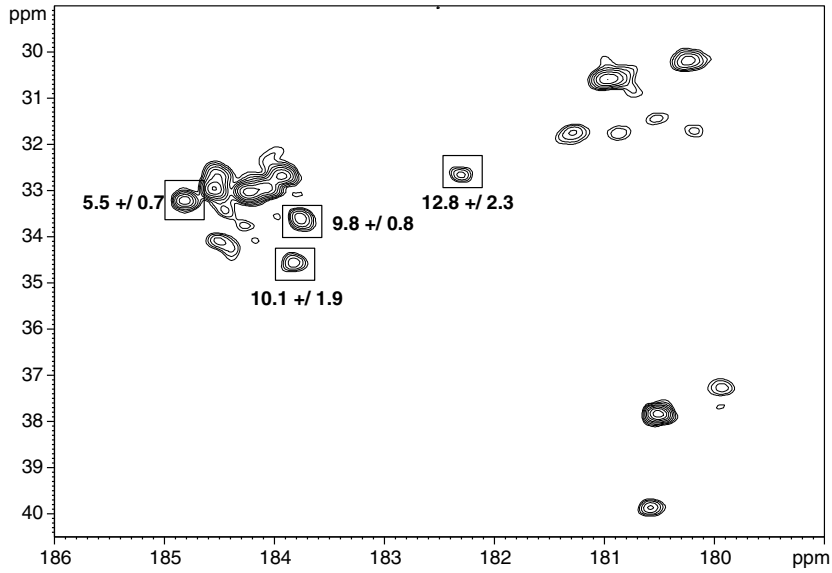

Fig. 5. Examples of side-chain ^{13}CO relaxation rates for 50% perdeuterated human Pin1 (163 residues), 0.7 mM at 18.8 T, 295 K. The spectral region is that of Glu side-chain ^{13}CO groups. The delay $\Delta = 1/4J_{\mathrm{CH}}$ selects for side-chain ^{13}CO groups adjacent to CHD methylene isotopomers. The spin-lock duration is 18 ms at 2.0 kHz rf-field strength. $R_{2,\mathrm{eff}}$ rate constants for the boxed cross-peaks are from use of Eq. (9) in the main text.

side-chain γ-^{13}C are pending, we already see a spread of $R_{2,\mathrm{eff}}$ values, suggesting that different side-chains experience different extents of local mobility. Moreover, Fig. 5 shows sufficient sensitivity to justify deeper analyses as described above for the smaller Pin1–WW domain, and suggests ^{13}C-detection method presented here should enable investigation of backbone Gly and side-chain ^{13}CO relaxation for medium-sized 50% perdeuterated proteins. Such labeling schemes are already routine for deuterium relaxation studies of methyl-bearing side-chains [7,8].

The ^{13}CO $R_{1\rho}$ relaxation measurements can be combined with ^{15}N R_1 and R_2 measurements to describe more collective aspects of fast (ps–ns) peptide plane dynamics. Examples are the semi-local dynamics analyses by Fischer et al. [15] and the 3-D Gaussian axial fluctuation (GAF) model of Brüschweiler and co-workers [18,38]. These methods exploit the fact that the ^{13}CO and ^{15}N relaxation rates probe angular fluctuations about distinct complementary axes, and can thus be combined to describe the local anisotropy of peptide plane motion.

The ^{13}CO $R_{1\rho}$ measurements can also probe μs–ms chemical exchange processes modulating the ^{13}CO chemical shift [34]. Although we have not done so here, the implicit frequency dependence of R_{ex} in Eq. (8) (which represents the additional transverse relaxation from chemical exchange) can be mapped by dispersion experiments that vary the strength of the effective spin-lock field [25,34]. This is achieved by varying the resonance offset, changing the rf-field strength, or both. Combining such dispersion measurements with those from ^{15}N, should provide a richer description of conformational exchange affecting the peptide plane.

Finally, we discuss the obvious advantage that our ^{13}C-detection approach avoids artifacts from incomplete water suppression. This is especially pertinent for backbone ^{13}CO groups. For example, one could measure ^{13}CO relaxation rates using an "out-and-back" HCACO strategy that detects signal on the ^{1}Hα proton. However, for proteins dissolved in >90% H_2O buffers, the residual H_2O signal can still hinder analyses of some Hα resonances, even with pulse-field-gradient coherence selection techniques. Moreover, studies of exchange dynamics often involve low temperature measurements using pulse-sequences with sustained pulsing on ^{1}H (e.g. to suppress cross-correlation and scalar coupling effects). This exacerbates radiation damping, whereby water suppression further suffers. ^{13}C-detection bypasses all of these potential problems.

5. Conclusion

We have introduced a direct ^{13}C-detection pulse scheme for the measurement of backbone and side-chain ^{13}CO relaxation parameters. The approach provides access to ^{13}CO groups that standard HNCO approaches cannot [3,33,34]. These include backbone ^{13}CO of residues preceding Pro residues, as well as side-chain carboxylic acid groups of Asp and Glu. Such ^{13}CO groups often participate in hydrogen bonds and electrostatic interactions important for protein–ligand recognition. Moreover, the ^{13}C-detected method can offer substantial advantages when investigating peptide linkages whose ^{15}N–^{1}H nuclei are broadened out by intermediate exchange, and hence, unobservable by more standard ^{15}N–^{1}H HSQC and HNCO-based methods. Such exchange often occurs in protein surface loops used for docking and catalysis. Hence, the ^{13}C-detection method here, which avoids the ^{15}N–^{1}H moiety entirely, can fill gaps inherent in more standard HNCO-based methods.

For very large proteins, the lack of aliphatic protons due to extremely high levels of perdeuteration (~90%) means our experiment is no longer viable. But, for those same proteins, our experiments can be particularly useful for studies of *ligand* mobility in complex with large proteins. Specifically, for labeled peptide ligands, then ^{13}C-labeled peptides can be complexed with highly deuterated protein [39,40] The ^{13}C-detected experiments then provide a unique means to profile residual mobility of the bound ligand. Work is in progress along these lines.

Acknowledgments

This work was supported in part by the ACS Petroleum Research Fund PRF # 44640-G4. We thank Dr. Tao Peng for useful discussions and critical reading of the manuscript.

References

[1] L.E. Kay, D.A. Torchia, A. Bax, Biochemistry 28 (1989) 8972–8979.
[2] G. Wagner, Curr. Opin. Struct. Biol. 3 (1993) 748–754.
[3] K.T. Dayie, G. Wagner, J. Am. Chem. Soc. 119 (1997) 7797–7806.
[4] L. Zeng, M.W.F. Fischer, E.R.P. Zuiderweg, J. Biomol. NMR 7 (1996) 157–162.
[5] S.L. Chang, N. Tjandra, J. Magn. Reson. 174 (2005) 43–53.
[6] T. Wang, D.S. Weaver, S. Cai, E.R. Zuiderweg, J. Biomol. NMR 36 (2006) 79–102.
[7] D.R. Muhandiram, T. Yamazaki, B.D. Sykes, L.E. Kay, J. Am. Chem. Soc. 117 (1995) 11536–11544.
[8] O. Millet, D.R. Muhandiram, N.R. Skrynnikov, L.E. Kay, J. Am. Chem. Soc. 124 (2002) 6439–6448.
[9] N.R. Skrynnikov, O. Millet, L.E. Kay, J. Am. Chem. Soc. 124 (2002) 6449–6460.
[10] V. Tugarinov, L.E. Kay, Chembiochem 6 (2005) 1567–1577.
[11] Z. Serber, C. Richter, V. Dötsch, Chembiochem 2 (2001) 247–251.
[12] Z. Serber, C. Richter, D. Moskau, J.-M. Bohlen, T. Gerfin, D. Marek, M. Häberli, L. Baselgia, F. Laukien, A.S. Stern, J.C. Hoch, V. Dötsch, J. Am. Chem. Soc. 122 (2000) 3554–3555.
[13] W. Bermel, I. Bertini, I.C. Felli, R. Kümmerle, R. Pierattelli, J. Magn. Reson. 178 (2006) 56–64.
[14] W. Bermel, I. Bertini, I.C. Felli, Y.M. Lee, C. Luchinat, R. Pierattelli, J. Am. Chem. Soc. 128 (2006) 3918–3919.
[15] M.W. Fischer, L. Zeng, A. Majumdar, E.R. Zuiderweg, Proc. Natl. Acad. Sci. USA 95 (1998) 8016–8019.
[16] J. Engelke, H. Rüterjans, J. Biomol. NMR 9 (1997) 63–78.
[17] P. Allard, T. Härd, J. Magn. Reson. 126 (1997) 48–57.
[18] S.F. Lienin, T. Bremi, B. Brutscher, R. Brüschweiler, R.R. Ernst, J. Am. Chem. Soc. 120 (1998) 9870–9879.
[19] T. Wang, K.K. Frederick, T.I. Igumenova, A.J. Wand, E.R. Zuiderweg, J. Am. Chem. Soc. 127 (2005) 828–829.
[20] L.E. Kay, M. Ikura, R. Tschudin, A. Bax, J. Magn. Reson. 89 (1990) 496–514.
[21] A. Zarrinpar, R.P. Bhattacharyya, W.A. Lim, Sci. STKE 2003 (2003) RE8.
[22] J.R. Schnell, H.J. Dyson, P.E. Wright, Annu. Rev. Biophys. Biomol. Struct. 33 (2004) 119–140.
[23] D.I. Freedberg, R. Ishima, J. Jacob, Y.X. Wang, I. Kustanovich, J.M. Louis, D.A. Torchia, Protein Sci. 11 (2002) 221–232.
[24] F.A.A. Mulder, R.A. de Graaf, R. Kaptein, R. Boelens, J. Magn. Reson. 131 (1998) 351–357.
[25] M. Akke, A.G. Palmer, J. Am. Chem. Soc. 118 (1996) 911–912.
[26] M. Ottiger, F. Delaglio, A. Bax, J. Magn. Reson. 131 (1998) 373–378.
[27] J.W. Peng, G. Wagner, J. Magn. Reson. 98 (1992) 308–322.
[28] T. Peng, J.S. Zintsmaster, A.T. Namanja, J.W. Peng, Nat. Struct. Mol. Biol. 14 (2007) 325–331.
[29] A.T. Namanja, T. Peng, J.S. Zintsmaster, A.C. Elson, M.G. Shakour, J.W. Peng, Structure 15 (2007) 313–327.
[30] A.J. Shaka, J. Keeler, Prog. NMR Spectrom. 19 (1987) 47–129.
[31] A.C. Wang, A. Bax, J. Biolmol. NMR 3 (1993) 715–720.
[32] J.W. Peng, J. Am. Chem. Soc. 52 (2003) 11116–11130.
[33] M.W.F. Fischer, L. Zeng, Y. Pang, W. Hu, A. Majumdar, E.R.P. Zuiderweg, J. Am. Chem. Soc. 119 (1997) 12629–12642.
[34] F.A.A. Mulder, M. Akke, Magn. Reson. Chem. 41 (2003) 853–865.
[35] K. Pervushin, A. Eletsky, J. Biomol. NMR 25 (2003) 147–152.
[36] P. Tompa, M. Fuxreiter, Trends Biochem. Sci. 33 (2008) 2–8.
[37] M. Fuxreiter, P. Tompa, I. Simon, Bioinformatics 23 (2007) 950–956.
[38] T. Bremi, R. Brüschweiler, J. Am. Chem. Soc. 119 (1997) 6672–6673.
[39] M.J. Berardi, C.L. Pendred, J.H. Bushweller, Biochemistry 37 (1998) 5849–5857.
[40] P.J. Finerty Jr., A.K. Mittermaier, R. Muhandiram, L.E. Kay, J.D. Forman-Kay, Biochemistry 44 (2005) 694–703.
[41] L. Emsley, G. Bodenhausen, J. Magn. Reson. 97 (1992) 135.
[42] D. Marion, M. Ikura, R. Tschudin, A. Bax, J. Magn. Reson. 85 (1989) 393–399.